Journal Pre-proof

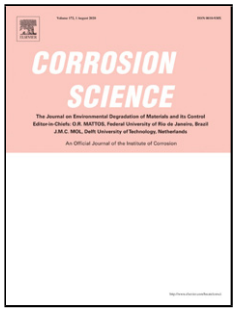

The differences in the corrosion product compositions of Methanogen-induced microbiologically influenced corrosion (Mi-MIC) between static and dynamic growth conditions

Biwen Annie An (Conceptualization) (Methodology) (Formal analysis) (Investigation) (Writing - original draft) (Writing - review and editing) (Visualization), Eric Deland (Conceptualization) (Methodology) (Formal analysis)<ce:contributor-role>investigation) (Writing - original draft) (Writing - review and editing) (Visualization), Oded Sobol (Methodology) (Formal analysis) (Resources) (Writing - review and editing), Jizheng Yao (Methodology) (Writing - review and editing) (Resources), Torben Lund Skovhus (Conceptualization) (Writing - review and editing), Andrea Koerdt (Conceptualization) (Visualization) (Writing - review and editing) (Supervision) (Project administration) (Funding acquisition)

PII: S0010-938X(20)32460-4

DOI: https://doi.org/10.1016/j.corsci.2020.109179

Reference: CS 109179

To appear in: *Corrosion Science*

Received Date: 27 June 2020

Revised Date: 21 November 2020

Accepted Date: 2 December 2020

Please cite this article as: An BA, Deland E, Sobol O, Yao J, Skovhus TL, Koerdt A, The differences in the corrosion product compositions of Methanogen-induced microbiologically influenced corrosion (Mi-MIC) between static and dynamic growth conditions, *Corrosion Science* (2020), doi: https://doi.org/10.1016/j.corsci.2020.109179

The differences in the corrosion product compositions of Methanogen-induced microbiologically influenced corrosion (Mi-MIC) between static and dynamic growth conditions.

Biwen Annie An[1*], Eric Deland[1*], Oded Sobol[1], Jizheng Yao[2], Torben Lund Skovhus[3], Andrea Koerdt[1]**

[1]Bundesanstalt für Materialforschung und -prüfung (BAM), Unter den Eichen 87, 12205, Berlin, Germany

[2] Sino-German Joint Research Lab for Space Biomaterials and Translational Technology, School of Life Sciences, Northwestern Polytechnical University, Xi'an, Shaanxi, 710072, China

[3] VIA University College, Chr. M. Østergaards Vej 4, DK-8700, Horsens, Denmark

[*] *These authors have contributed equally to the work*

**** Correspondence:**
Corresponding Author
Andrea.koerdt@bam.de

Keywords: Carbon steel, modelling studies, SIMS, SEM, reactor conditions, microbiological corrosion

Highlight

- Dominant corrosion product of corrosive methanogens is not siderite
- Methanogenesis may affect the nucleation process of carbon-oxygen compounds
- Methanogens induce high corrosion rates (0.72 mm/yr) under dynamic environments
- Growth conditions influence the corrosion process of methanogens

Abstract

Currently, corrosion rates (CR) and/or corrosion products (CP) obtained for methanogen-induced microbiologically influenced corrosion (Mi-MIC) on carbon steel are mainly analyzed from static-incubations. By using a multiport-flow-column, much higher CRs (0.72 mm/yr) were observed, indicating static-incubations are not suitable for determining the corrosive potential of Mi-MIC. With the combination of various analytical methods (ToF-SIMS/SEM-EDS/SEM-FIB) and contrary to previously published data, we observed that CPs contained phosphorus, oxygen, magnesium, calcium and iron but lacked carbon-related species (e.g. siderite). Overall, siderite nucleation is disrupted by methanogens, as they convert aqueous bicarbonate into carbon dioxide for methanogenesis resulting in increased localized corrosion.

Introduction

Corrosion is a costly phenomenon found in several industries as it often leads to detrimental infrastructure breakdowns, i.e. pipeline failures and eventual spills. The annual global cost of corrosion is estimated to be 3 % to 4 % of each country's Gross Domestic Product (GDP), or US$2.5 trillion [1], not including costs associated with environmental consequences, i.e. remediation costs [2]. To establish effective preventative strategies, all areas of corrosion science, including material science, electrochemistry and biology must be considered. One limiting factor for effective corrosion monitoring is microbiologically influenced corrosion (MIC). In this sense, carbon steel (> 98% Fe^o) is one of the most used infrastructure materials due to its favorable properties and its low-cost [3]. Under anoxic conditions, carbon steel is highly susceptible to MIC, for instance by serving as an electron donor [4, 5]. Due to the diverse microbial communities and complex environmental condition, i.e. temperature, pH and pressure, MIC is a highly unpredictable process [4, 5]. Only in the last years several key microorganisms, next to sulfate-reducing bacteria (SRB) have been identified, including iron-reducing bacteria, iron-oxidizing bacteria, acetogenic bacteria and methanogenic archaea [4-10]. Moreover, to the present, two types of MIC have been proposed: indirect MIC and direct MIC [5]. Indirect MIC occurs when microorganisms produce metabolites which are corrosive to the metal, like acids from fermentative microorganisms or H_2S from SRB [5]. In direct MIC, microorganisms use the metal as an electron donor, i.e. carbon steel [5]. MIC is often identified through the formation of pits, which are localized and difficult to predict [11].

For lithotrophic SRB or direct MIC-SRB, electrons are directly withdrawn from the steel surface through membrane-bound redox proteins for sulfate reduction (Equation 1) [5].

$$\text{Equation 1 } 4Fe^o + SO_4^{2-} + 3HCO_3^- + 5H^+ \rightarrow FeS + 3FeCO_3 + 4H_2O$$

The formation of iron sulfide (FeS) can increase the corrosion rate by generating localized corrosion cells on the steel surface [12]. In addition to SRB, methanogens are also capable of direct MIC by using elemental iron as an electron source for methanogenesis (Equation 2) [6, 13-16]. However limited information is available on the corrosion mechanism of methanogen-induced MIC (Mi-MIC).

$$\text{Equation 2 } 8H^+ + 4Fe^o + CO_2 \rightarrow CH_4 + 4Fe^{2+} + 2H_2O$$

Recently, corrosion mechanisms of *Methanococcus maripaludis* OS7 and KA1 were proposed by comparing genomic differences between iron-grown strains and hydrogen-grown strains [16], where a corrosive genomic island or MIC-island was identified [16]. The MIC-island was identified to be an unstable 12 kb gene segment encoding a secretion system and a [NiFe] hydrogenase, which is supposed to attach to the metal surface upon secretion, allowing direct metal oxidation and hydrogen production (Equation 3) [16, 17]. Produced hydrogen is further consumed in the process of methanogenesis [16].

$$\text{Equation 3 } 2H^+ + Fe^o \leftrightarrow H_2 + Fe^{2+}$$

However, the production and secretion of genes encoded in the MIC-island by corrosive methanogens were only proposed for members of *M. maripaludis*. Other corrosive methanogens, such as members of *Methanobacterium* and Baltic-*Methanosarcina* [13, 18, 19], can directly utilize elemental iron for methanogenesis with low H_2-affinity, but the mechanism

remains unclear [18, 20]. Unlike SRB-induced MIC, Mi-MIC was often seen as minimal or preventative due to the formation of proposed corrosion products: siderite ($FeCO_3$) [15, 21].

Siderite is an electrically insulating mineral and is proposed to be the sole corrosion product of Mi-MIC [20-23]. The low corrosion rates reported for Mi-MIC (between 0.02 to 0.065 mm/yr), in different laboratories grown as static culture [6, 15, 24] further reinforced siderite as the main culprit for the low corrosivity of methanogens. However, the formation of siderite is directly dependent on the availabilities of ferrous and carbonate ions in the environment (Equation 4) [25-27]. The stability of the siderite structure is based on the solubility factor or supersaturation level (K_{sp}; Equation 4) [26].

$$\text{Equation 4} \qquad S=\frac{[Fe^{2+}][CO_3^{2-}]}{K_{sp}}$$

Siderite nuclei can only be formed above the saturation level and continuously to nucleate if supersaturation is maintained [26]. Stability of the supersaturation level relies heavily on several factors, including pH, pressure, temperature, flow and salinity [25-27]. For example, higher ionic strength results in delayed nucleation formation of siderite due to increase in the supersaturation factor (Equation 4). Furthermore, in anoxic, iron-rich, CO_2-rich and seawater conditions, i.e. ancient Archaeon sea, additional ferric compounds such as magnetite (Fe_3O_4) and greenalite ((Fe^{2+}, Fe^{3+})$_{2-3}Si_2O_5OH_4$.) will form [28]. Under these conditions, siderite compounds could be partially replaced by magnetite (Equation 5) [28]:

$$\text{Equation 3} \qquad 3FeCO_3 + H_2O \rightarrow Fe_3O_4 + 3CO_2 + H_2$$

In CO_2-rich environments without microbial influences, additional crystalline solid phases such as magnetite and chukanovite are also formed [25, 27] due to the changes in the supersaturation level of siderite. In the presence of other ions, i.e. Mg^{2+} and Ca^{2+}, nucleation of the siderite crystal structure will transform, resulting in the formations of magnesium carbonate ($MgCO_3$), calcium carbonate ($CaCO_3$), or Fe- (Mg or Ca)-x solid phases [25, 27]. Thus, formation of solely siderite as a biogenic corrosion product for Mi-MIC remains highly questionable.

Currently, all identified corrosive methanogens are marine archaea and at this salinity, the formation of siderite or the saturation index (Equation 4) should be affected. Only recently it was realized that MIC should be investigated under dynamic conditions since static enrichments might not simulate the natural conditions. In a study recently published, we showed that the marine methanogenic strain *Methanobacterium-like* IM1, grown under dynamic conditions, leads to higher corrosion rates than previously assumed (0.52 mm/yr). Based on this, the purpose of the following contribution is to realize if 1) similar patterns are observed for other corrosive methanogens, 2) methanogens indeed only produce siderite as the corrosion product and 3) the resulting corrosion products differ when grown under static or dynamic conditions. To answer those questions and to verify the corrosion products of methanogens, experiments conducted using the flow system were compared with traditional serum bottle enrichments. Additionally, multiple surface analysis techniques were incorporated to create a comprehensive overview on the corrosion products. Overall, the results of the study provided an interesting perspective on the corrosion mechanisms of methanogens with increased geochemical, biological and industrial benefits.

Materials and Method

Strains, media and culturing conditions

Two methanogenic archaea strains *Methanococcus maripaludis* Mic1c10 (NBRC #105639, NITE Biological Resource Center, Japan) and *M. maripaludis* KA1 (NBRC #102054, NITE Biological Resource Center, Japan) were grown in anoxic artificial sea water medium (ASW) [29] at 30°C buffered with CO_2/HCO_3^- under anoxic headspace (80% N_2 and 20% CO_2, v/v). Additional supplements were added post-autoclaving and were described previously [17] and reduced using cysteine (1 mM) and sodium sulfide (1 mM) [29]. Acid-sterilized (NACE protocol SP0775-2013) steel coupons (Table 1) and carbon steel beads (Table 1; average weight: 55.22 mg ± 0.011 mg) were used as electron donors. Each culture bottle (50 mL ASW) contained three pre-treated coupons and biological replicates were conducted in triplicates (abiotic controls were conducted in duplicates) for 14 days at 30 °C. Growth was monitored by measuring the methane concentration in headspace (8890 GC System equipped with a thermal conductivity detector, Teckso GmBH, Germany), using methods previously described [17]. The fully-grown cultures (30-35%) were used to inoculate the multiport flow columns (MFC).

Table 1 Iron specimen chemical properties according to manufacturer data

Iron specimen	Fe (%)	Mn (%)	Si (%)	C (%)	P (%)	S (%)	Dimension	Company
Carbon steel coupon	99.5	0.3	0.1	< 0.08	< 0.04	< 0.05	0.8 cm x 0.8 cm x 0.8 x cm	Goodfellow GmbH, Hamburg, Germany
Carbon steel bead	99.18-99.62	0.3-0.6	< 0.1	0.08-0.13	< 0.04	< 0.05	Ø = 0.238 cm	Simply bearings, England

Multiport flow-column set-up and corrosion rate calculation

A multiport flow column (MFC) set-up was constructed as previously described [17]. The carbon steel beads served as the electron donors (20 sterile beads per section). The beads were acid sterilized using the same NACE protocol [30]. Each section of the column was separated using glass beads of similar sizes to carbon steel beads. Additionally, a sterilized carbon steel coupon was inserted between sections 2 and 3 for surface analyses. The pore volumes (PV) of the columns were calculated based on the differences in weights between the media-flooded columns and the dry columns [17]. Around 0.5 PV of cultures were used as the inocula. In order for the cells to establish an initial biofilm on the iron surface, the columns were incubated anaerobically for 3.5 days at 30 °C without any flow. After 3.5 days, fresh medium (ASW) were continuously introduced into the columns. The columns incubated with methanogens were conducted in triplicates and abiotic controls were conducted in duplicates. The daily flow rate of the system was 45 mL, or 1.2 PV. To measure methane concentration, a sealed serum bottle was connected to the effluent port of the columns and the headspace was analyzed using the same gas chromatography. Post experiment, the columns were sectionally deconstructed. The beads were cleaned using the same NACE protocol [31]. The corrosion rates of the carbon steel beads were calculated using the weight loss method by subtracting the final weight with the initial weights of each bead. The rates were then calculated with the same formula as described previously [17]. Statistical analyses (Origin (Pro), Version 2020 OriginLab Corporation, Northampton, MA, USA) of corrosion rates were performed [17]

Surface analyses and corrosion product identification

Time of Flight - Secondary Ion Mass Spectrometry (ToF-SIMS)

At the end of each batch culture experiment and flow-through system experiment, coupons were washed once with filter sterilized PBS/dH_2O (1:2, v/v), then incubated overnight at 4°C in 1 mL 2.5% glutaraldehyde solution for fixation of microorganisms. Subsequently, the coupons were washed first with filter sterilized PBS/dH_2O (1:2, v/v) for 5 min, then for another 5 min in sterilized dH_2O. The dehydration of coupons was carried out using different ethanol dilutions (30% [30 min], 50% [30 min], 70% [30 min], 80% [60 min], 90% [60 min] (v/v) and absolute [60 min]) and dried with N_2 gas.

The exposed surface of the coupon was sputtered with gold (15 nm, Quorum Technologies, UK). The coupons were then horizontally embedded in epoxy resin and polished with SiC paper with increasing grits (grit 320 to grit 2000) to observe the cross section. The gold layer served as a reference point to distinguish between the corrosion layer and the epoxy for the ToF-SIMS analyses of the cross-sections.

ToF-SIMS analyses were carried out using a ToF-SIMS IV instrument (IONTOF GmbH, Münster, Germany). Investigations were performed in the collimated burst alignment (CBA) mode using a 25 kV Bi^{1+} as primary ion source, enabling a good spatial resolution down to 100 nm per pixel [32]. The analyses were performed in the negative and positive polarities. The region of interest (ROI) of 100 x 100 (µm) was scanned in sawtooth mode with 512 x 512 pixels and one shot/pixel. The analyzed region was sputtered for 120 seconds with another specie before each analysis in order to remove surface contaminations and to enhance the secondary ion yield in each analysis mode. For the negative mode, the ROI was sputtered with a 3 kV Cs^+ ions and for the positive mode with 3 kV O_2^+ ions. The sputtered crater size was adjusted to 500 x 500 (µm), where the analyzed region is in the center. For charge compensation, a low energy electron flood gun (20 V) was used after standard readjustment of the surface potential for the measurement.

SEM and FIB-SEM

Metal coupons coated with gold (15 nm) were used for scanning electron microscope imaging (SEM; Zeiss EVO MA10; 12kV). Energy dispersive X-ray spectroscopy (EDS) measurements were conducted using the Pathfinder Basecamp EDS system (Thermo Scientific, Germany) equipped with silicon-drift detector (area: 30 mm^2, resolution 129 eV, UltraDry EDS detector, Thermo Scientific, Germany). A separate set of metal coupons were subjected to focused ion beam scanning electron microscopy (FIB-SEM). The metal coupons were coated with gold (15 nm) to increase surface electric conductivity. Platinum (~5 nm) was then deposited on each cross-section using ion beam induced deposition (30 kV, Ga^+ ions) as part of the standard FIB procedure. Cross-sections were sliced by FIB (FEI 200xP, Thermo Fisher Scientific, Germany) and imaged by SEM at an angle of 52° to the surface (5 kV, secondary electron detector).

Data analysis

Principal component analysis (PCA) and data fusion

ToF-SIMS data were processed using ImageLab (Epina Softwareentwicklungs-und Vertriebs-GmbH, Retz, Austria). The application of principal component analysis (PCA) enabled to extract a correlation between the different fragments (e.g. m/z=1, H, m/z=13, CH, m/z=14, CH_2, etc.). PCA has been applied on the data from the analyses acquired in the negative mode. For each dataset, several m/z were selected in order to build the spectral descriptors-list for the PCA. Before performing PCA, the raw data were normalized to the total intensity to minimize matrix effects and the image data was shift corrected to remove the drift during the analyses. In addition, the data was scaled and mean centered prior to PCA. ImageLab was then used for the fusion of the data with the SEM images taken from the same region on the cross-section.

Results

Corrosion rate distribution and surface analyses of *M. maripaludis* in multiport flow test column

Corrosion capacities of *M. maripaludis* KA1 and Mic1c10 were evaluated using the unique multiport flow system [17]. Direction of the flow was unidirectional from bottom to top (section 1 to 6). Average corrosion rate for the abiotic control of the whole column was 0.063 ±0.054 mm/yr, with highest corrosion rates at sections 1 and section 6 (Figure 1). At the fastest, beads lost more than 1% of their initial weight and at the slowest beads lost less than 1% of their initial weight. Proportions were further calculated [17], and three sections of the abiotic control had 0% of fast-corroding beads (data not shown). In comparison, the average corrosion rate for *M. maripaludis* KA1 was 0.081 ± 0.074 mm/yr with the highest corrosion rates in sections 5 and 6 (Figure 1). The beads with the highest individual corrosion rates were 0.36 and 0.38 mm/yr, which were identified from the regions with the highest average corrosion. Average corrosion rates of *M. maripaludis* KA1 at sections 5 and 6 were 0.10 ± 0.11 mm/yr and 0.14 ± 0.098 mm/yr, respectively (Supplementary Table 1). Sections 5 and 6 also had the highest proportions of fast-corroding beads, which were 21% and 28%, respectively (data not shown). Surface analyses of corroded beads appeared visual severe roughness and pitting, in comparison to the beads with 0 mm/yr (Figure 2 A to F). Other sections were predominately slow-corroding bead (78 to 97 %) and were statistically significantly different from the control.

On the contrary, carbon steel beads were mostly corroded at the bottom sections of the columns incubated with *M. maripaludis* Mic1c10 (Figure 1). The average corrosion rate of *M. maripaludis* Mic1c10 was 0.14 ± 0.1 mm/yr, which is 1.7 and 2.2 times more than that of *M. maripaludis* KA1 and abiotic control, respectively. All sections of *M. maripaludis* Mic1c10 were dominated by fast-corroding beads (> 50%) and highest in section 6 (81.7 %, data not shown). Sections 1, 2, and 6 had the highest corrosion, with corrosion rates of 0.15 ± 0.12 mm/yr, 0.18 ± 0.17 mm/yr and 0.15 ± 0.045mm/yr, respectively. The beads with the highest corrosion rates were in sections 1 and 2 with 0.60 and 0.72 mm/yr, respectively. Surface morphology of these beads showed severe pitting and roughness (Figure 2 G to J). Corrosion rates of all Mic1c10 column sections were statistically different from the control, indicating minimal abiotic corrosion.

Cross-section comparisons between static and column carbon steel coupons

Cross sections of abiotic control, *M. maripaludis* KA1 and Mic1c10 were compared between static and flow column treated carbon steel coupons (Figure 3). FIB-SEM images were used to examine and compare subsurface structures close to the metal surface. In the abiotic controls a very thin corrosion layer was observed under both static and flow conditions (Figure 3 A and D); the layer thickness was at maximum 1 µm in both cases. One clear difference between the controls was the surface structure of the corrosion layer which appeared to be flat. In comparison, the surface under flowing conditions appeared to be uneven and rough. Similar roughness has been observed with *M. maripaludis* KA1 under flow conditions. However, the thickness of the corrosion deposits was significantly higher, and reached a thickness of 12 µm. This layer was not compact but rather multi-layered porous and contained large number of cavities. These cavities were partially connected to each other and appeared to have a connection from the metal surface to the external medium through an open tunnel. The transition from the corrosion product layer to the metal surface appeared to be uneven as well (Figure 3 E), which might indicate that here pitting corrosion is a preferable process. Under static conditions, the corrosion layer of *M. maripaludis* KA1, which was only a few µm in size, can rather be described as a uniform/ two-layer matrix interface (Figure 3 B). This appearance

was comparable to that described earlier by Uchiyama et al [21]. In *M. maripaludis* Mic1c10 the corrosion layer had a unique appearance. The thickness of the layer in both cases, static and flow, was the highest compared to all other samples with 10 and 15 µm respectively. The deposits on the metal appeared to be dense and compact in both cases (Figure 3 C and F). In the case of *M. maripaludis* Mic1c10 under flow conditions, the transition to the metal could not be visualized due to the corrosion layer thickness (Figure 3 F). In the case of *M. maripaludis* Mic1c10 under flow conditions (Figure 3 F), a hollow free volume has been observed, indicating that below the compact top-layer a more porous-layer could be present. The most prominent feature of *M. maripaludis* Mic1c10, under both static and flow conditions, is that the deposits appeared uneven as well.

Surface chemical analyses with ToF-SIMS and EDS

The corrosion layers of the coupons incubated with *M. maripaludis* KA1 under flow conditions contained oxygen, phosphorus, magnesium and iron (Figure 4 D, E, G and H). The correlation between oxygen, phosphorus, magnesium and partially iron at the same location, has indicated a possible underlying interaction between these elements. These signals were equally distributed in the corrosion layer of the coupon incubated in the column system with *M. maripaludis* KA1, resulting in regional accumulations (Figure 4 E, G and H). For the samples under flow conditions, EDS measurements revealed no calcium signals for the coupon incubated with *M. maripaludis* KA1 (Figure 4 C). ToF-SIMS measurement in the positive mode showed for the same spot signals for the m/z =40, which is attributed to calcium (Supplementary Figure 5 A). The corrosion layer of the samples incubated with *M. maripaludis* KA1 under static culture conditions were unequally distributed with several regions enriched with phosphorus, oxygen and magnesium (Figure 5 E, G and H). Whereas, EDS as well as positive ToF-SIMS measurements showed, that the corrosion layer of the coupon incubated with *M. maripaludis* KA1 from the static culture contains calcium (Figure 5 C and Supplementary Figure 5 B).

On the contrary, the corrosion layers of the coupon incubated with *M. maripaludis* Mic1c10 contained oxygen, phosphorus, magnesium, iron and calcium (Figure 6 C-E, G, H and Figure 7 C-E, G, H). ToF-SIMS measurements (shown in the Supplementary Figure 6 A, B) further confirmed that calcium was present in the corrosion layer of the coupon incubated with *M. maripaludis* Mic1c10. Magnesium has been detected to a lower extent by ToF-SIMS (m/z=23) and appeared to be present in the corrosion layers (Supplementary Figure 6 A, B). A correlation between oxygen, phosphorus, magnesium, iron and calcium has been observed at the same location, similar to the coupons incubated with *M. maripaludis* KA1. The distribution of the elemental signals has indicated a possible relationship between these elements. EDS images of coupons incubated with *M. maripaludis* Mic1c10 revealed that regions with high magnesium and phosphorus content did not show calcium and iron signals (Figures 7 C-E and G). The corrosion layers of the abiotic controls also contained oxygen and phosphorus (Supplementary Figure 1 G, H). The corrosion products of the abiotic controls formed under static conditions, appeared to contain magnesium (Supplementary Figure 2 E) as opposed was calcium, detected in the sample of the column system (Supplementary Figure 1 E).

The examination of the corrosion products by EDS showed that carbon is present in the samples incubated with *M. maripaludis* KA1 under static conditions (Figure 5B). Contrary to the previously published studies, which described siderites as the only corrosion product of the methanogens, no carbon could be detected for *M. maripaludis* Mic1c10, under both tested conditions (Figure 6 B and 7 B), and for *M. maripaludis* KA1 under column conditions (Figure 4 B). Contradictory to the above-mentioned EDS result with *M. maripaludis* KA1 in the column

system, the ToF-SIMS results showed carbon in the corrosion products. However, in this case it is assumed to be associated with hydrogen, which has been confirmed by Principal Component Analysis (PCA) (Supplementary Figure 3). These analyses indicated that the C-H compounds are unevenly distributed within the corrosion layer.

Contrary to the coupons from the static system, analyses of the coupon incubated with *M. maripaludis* KA1 in the column system showed by both ToF-SIMS and EDS measurements no correlation between the signals of carbon and oxygen (Figure 4 B, H). The measurements of static incubated *M. maripaludis* KA1-coupons indicate that there are areas in the corrosion layer, where carbon and oxygen could be associated with each other (Figure 5 B, H). For the *M. maripaludis* Mic1c10, ToF-SIMS and EDS images indicated that in the column incubated coupon the corrosion layer does not contain carbon (Figure 6 B and Figure 9 B) whereas the corrosion layer of the static incubated coupon a correlation between carbon and oxygen has been observed (Figure 7 B, H).

Sulfur has showed distinct differences, using both ToF-SIMS and EDS. In this case, in the column system with *M. maripaludis* KA1, coupons showed accumulations of sulfur at certain regions (Figure 4 F and Figure 8 A). These regions are visible in the metal bulk and in the intermediate space of the oxygen-rich corrosion layer. The EDS images also show that sulfur and iron are associated with each other, which can be concluded from the correlation of both signals (Figure 4 D, F and Supplementary Figure 4). As another observation by EDS and ToF-SIMS, sulfur is present to a very low extent in the coupons incubated under static conditions with *M. maripaludis* KA1 (Figure 5 F and Figure 8 B). For coupons in the column system and static system, which were incubated with *M. maripaludis* Mic1c10, EDS images showed an even distribution of sulfur in the corrosion layer (Figure 6 F and Figure 7 F). However, this could not be confirmed by ToF-SIMS analysis (Figure 9 A and B). In all abiotic controls no sulfur has been detected (Supplementary Figure 1F and 2F. A and B).

Discussion

Results of the corrosion analyses of *M. maripaludis* KA1 and Mic1c10 suggest high corrosion potential under flow conditions compared to static incubations. This finding resonates previous reports on *Methanobacterium* IM1 [17]. Both results suggest that microbiologically influenced corrosion induced by methanogens (Mi-MIC) were ineffectively represented by static incubations.

MIC is a local and highly unpredictable process. This corrosion process might be manifested differently in each region of the metal, in other words, one region of the metal might be affected differently from the others. Thus, surface sensitive techniques such as ToF-SIMS, focusing on elemental mapping of the corrosion layer are more suitable to study the formed corrosion layers within the MIC process. ToF-SIMS provides a qualitative information about the distribution of all elements at the surface. Despite the ability to detect light elements, ToF-SIMS analysis conducted in the CBA mode has a relatively low mass resolution which is compromised in the present work by SEM-EDS measurements. EDS can provide a quantitative elemental distribution of iron, magnesium and calcium with a better mass resolution but limited with the detection of organic molecules, light elements and related fragmentation of molecules containing heavier elements.

ToF-SIMS and EDS measurements of Mi-MIC corrosion layers, have shown that the composition is much more complex than previously described [21]. ToF-SIMS measurements indicated that all corrosion layers (including the abiotic controls), contain phosphorus-oxygen compounds, such as phosphate (PO_4^-). The corrosion mechanism of *M. maripaludis* has been assumed to be stimulated by the secretion of MIC-associated hydrogenase through the TatA/TatC pathway encoded in the 'MIC island' genomic region [16, 33, 34]. The MIC hydrogenase has not been isolated, but the cell-free supernatant of *M. maripaludis* on iron showed hydrogen production [33]. The specific secretion mechanism of MIC hydrogenase and its presence in *M. maripaludis* Mic1c10 remain under investigation. However, regardless of the secretion pathway, the presence of extracellular hydrogenase stimulates the formation of iron-phosphate species containing vivianite [35]. The relationship between hydrogenase and iron-phosphorus compounds are even more complicated due to the instability of hydrogenase under different environmental conditions i.e. phosphate concentration, hydrogenase concentration or environmental stress [35]. PO_4^- ions are complex ions and can be ionized to several species [36, 37]. When PO_4^- is ionized, various forms of phosphoric ions will be produced, mostly PO_2^- and PO_3^- [36, 37]. In addition, one must consider the fragmentation that occurs during ToF-SIMS analysis and the probability to detect each of these species. Therefore, PO_4^- ions were mostly undetected unlike PO_2^- and PO_3^-. Additionally, Fe-P-O fragments such as $Fe_{(1-3)}PO_{(1-4)}^-$ could not be detected, because of the complexity of these ions, which are often ionized into several species, similarly to PO_4^- ions. Currently, there is a limited number of reports on the involvement of extracted hydrogenase on iron corrosion [33, 35, 38, 39], and little information is available on any corrosion product implications. Nonetheless, the presences of PO_2^- and PO_3^- has indicated on the formation of phosphoric corrosion species that were unknown previously for methanogen-induced MIC.

Signals from other elemental species, including sulfur, magnesium, calcium and oxygen were detected throughout the corrosion layers. EDS measurements showed that all corrosion layers except the corrosion layers of the abiotic controls, contained sulfur. Accumulations at the metal-

corrosion interface have been detected for carbon steel coupons which were incubated with KA1 extracted from the multiport column system. The sulfur accumulation has been confirmed by ToF-SIMS analyses, with sulfur/dioxygen showing different behaviors. All measurements have shown that iron and sulfur are associated with each other (Supplementary Figure 4) and possibly forming FeS fragments, a conductive compound [40]. Furthermore, EDS measurements have indicated an abundance of oxygen signals. With regards to that, it was reported that under anaerobic aqueous conditions, magnetite (Fe_3O_4) will be formed abiotically (Figure 11) [25], which is considered as a semi-conductive oxide often formed close to the metal surface [25]. Based on the FIB-SEM images of the *M. maripaludis* KA1 and Mic1c10 (Figure 3), the corrosion layer close to the metal surface appear differently than the layer above and separated by large intermittent gaps. Additionally, it was reported that under flow conditions, the presence of ligands, such as phosphate, led to the mineralization of magnetite [41]. The oxidation and reduction processes of magnetite in marine environments is also closely related to anaerobic biofilms [42]. Generally, magnetic level in marine sediments is closely related to the concentration of magnetite, which decreases drastically at the sulfate-methane transition zone, where methane concentration depletes [43]. In this context, it is known that the presence of magnetite greatly enhances methanogenesis [43-45]. However, further investigations on the involvements of hydrogenase and methanogen on magnetite production are necessary.

Carbonate (CO_3^-), similar to phosphorus-oxygen compounds, is also a ligand molecule capable of ionizing into different species as a function of pH and enzymatic activities [41]. In this context, signals of ($FeCO_3$) were represented by CO^- (m/z = 28), CO_2^- (m/z = 44), CO_3^- (m/z = 60) ions, as well as the Fe-associated carbon-oxygen compounds. However, precise $CO_{(1-3)}^-$ signals could not be obtained in any of the ToF-SIMS measurements. Considering the CBA analysis mode in the SIMS measurements, CO^- and Si^- have similar masses (m/z = 28) and might overlap in the spectrum, in addition, the carbon steel coupons are assumed to contain traces of silicon originating from the sample preparation. Due to the high sensitivity of ToF-SIMS to trace elements, the distinction between these two fragments was difficult. Also signals of magnesium and calcium did not coincide with carbon. It was reported that under carbonated conditions, mineral scales containing $MgCO_3$ and $CaCO_3$ can also form. Presences of divalent cations also stimulate the formation of compounds such as chukanovite ($Fe_2(OH)_2(CO_3)$), allowing a transient formation of $(Fe,Mg,Ca)CO_3$ solid solutions [26], which could not be detected. Nevertheless, no correlation was concluded between carbon and oxygen indicating siderite is not the main corrosion product of Mi-MIC contrary to previous publications [21].

In the present, siderite is known as the sole corrosion product of *M. maripaludis* or Mi-MIC. However, as shown here, signals of carbon, carbon-oxygen and iron-carbon were lacking. The formation of siderite is dependent on several factors, including the concentrations of CO_2, HCO_3^-, pH, salinity, temperature and flow [25, 27]. The supersaturation state of iron-carbonate is critical for the formation of siderite by allowing the nucleation of the crystallized structure and sub sequential particle growths [26]. If supersaturation state is not reached, dissolution of partially formed Fe-CO_3 [26] will occur. Under abiotic CO_2-rich conditions [46], formation of mild carbonic acid will result in iron dissolution at the anode causing corrosion. An excess of Fe^{2+} and CO_3^{2-} leads to the formation of siderite [26, 46]. The precipitation of siderite is susceptible to external disturbances and its nucleation requires a long induction time [47]. Based on presented data, under CO_2 supplemented methanogenic conditions, signals of carbon-oxygen were detected to a low extent. This result correlates with previous findings, where siderite formation was considered to be a possible corrosion product of corrosive methanogens

under stable laboratory conditions [21]. However, the detected signals of iron-carbon-oxygen were very weak in stationary cultures and were mostly absent in flow-column samples. The goal of the multiport-column experiment was to mimic natural marine conditions by supplementing in-situ methanogenic cells with artificial seawater containing bicarbonate. Based on our current results, a corrosion product deposition mechanism for methanogens is proposed (Figure 11).

Equation 7 $CO_2 + H_2O \leftrightarrow H_2CO_3 \leftrightarrow H^+ + HCO_3^- \leftrightarrow 2H^+ + CO_3^{2-}$

Typically, CO_2 dissolves into bicarbonate and carbonic acid upon entrance into the aquatic system (Equation 7) [43] and the lack of available gaseous CO_2 will require the activities of the carbonic anhydrase to revert bicarbonate back to CO_2 for methanogenesis (Figure 11). Increased activities of methanogens may disrupt the level of available aqueous carbonate for siderite nucleation, hence the lack of iron-carbonate signals. However, the corrosion mechanism of methanogens require further experimental verifications as many of the important aspects are still unknown, such as the impact of environmental fluctuations, i.e. pH and temperature changes, on the corrosion product formation. Incorporations of microsensors that identifies near surface reactions, i.e. hydrogen evolution, will be highly beneficial to uncover any underlying mechanisms. Additionally, genetic mutants of *M. maripaludis* lacking the carbonic anhydrase enzyme will further verify the role of carbonates on the corrosion mechanism of methanogens. Lastly, techniques allowing continuous surface imaging under anaerobic condition, such as specialized anaerobic flow cell chambers for confocal microscopy or environmental scanning electron microscopy (ESEM) will be useful to study the corrosion mechanisms of Mi-MIC.

Conclusion

Overall, methanogen-induced microbiologically influenced corrosion is a highly versatile process with complex underlying corrosion mechanisms. Our multiport-flow columns indicated that methanogens exhibit high corrosion potential while producing complex corrosion products independent from siderites. Additional analyses of the corrosion products as a function of distance from the injection site are required to uncover the corrosion mechanisms of Mi-MIC. Therefore, there is a clear need for a future work with the focus on integrating *in-situ* measurements of methanogen-induced MIC under SEM using extracted MIC hydrogenases and cells.

Data availability

The raw/processed data required to reproduce these findings can be shared upon request.

Author Contributions
ED and BA: Conceptualization, methodology, formal analysis, investigation, writing (original drafting and editing) and visualization. Both authors contributed equally to the article
OS: Methodology, formal analysis, resources and writing (reviewing & editing)
JZY: Methodology, writing (reviewing and editing) and resources
TLS: Conceptualization and writing (reviewing & editing),
AK: Conceptualization, visualization, writing (reviewing & editing), supervision, project administration and funding acquisition

Funding

This work was supported by the internal funds of the BAM provided through the MIC project and a corresponding investment in a range of microbiologically controlled environmental simulation facilities “MaUS kommt aus der Black Box”.

Declaration of interests

The authors declare that they have no known competing financial interests or personal relationships that could have appeared to influence the work reported in this paper.

Acknowledgments

Many thanks to Dr. Leonardo Agudo Jácome, René Hesse and Christiane Weimann for their assistances with scanning electron microscopy and energy-dispersive X-ray spectroscopy. We are also grateful to Dr. Adam Michalchuk for sharing his expertise on crystallography. Many thanks to Dr. Andreas Röhsler, who generously provided his expertise and assistance on ToF-SIMS analyses. We are also immensely grateful to Dr. Ozlem Ozcan for her comments on an earlier version of the manuscript. Lastly, we are very grateful for the supports from our colleagues in the Department 4.1 throughout our research.

References

[1] G. Koch, Cost of corrosion, in: A.M. El-Sherik (Ed.), Trends in Oil and Gas Corrosion Research and Technologies, Woodhead Publishing2017, pp. 3-30.10.1016/b978-0-08-101105-8.00001-2

[2] G. Koch, J. Varney, N. Thompson, O. Moghissi, M. Gould, J. Payer, International measures of prevention, application, and economics of corrosion technologies study, NACE International, 2016,

[3] D. Dwivedi, K.R. Lepko, T. Becker, Carbon steel corrosion: a review of key surface properties and characterization methods, RSC Adv 7 (2017) 4580-4610.10.1039/c6ra25094g

[4] D. An, X. Dong, A. An, H.S. Park, M. Strous, G. Voordouw, Metagenomic Analysis Indicates Epsilonproteobacteria as a Potential Cause of Microbial Corrosion in Pipelines Injected with Bisulfite., Frontiers in Microbiology 7 (2016) 28.10.3389/fmicb.2016.00028

[5] D. Enning, J. Garrelfs, Corrosion of iron by sulfate-reducing bacteria: New views of an old problem, Applied and Environmental Microbiology 80 (2014) 1226-1236.10.1128/AEM.02848-13

[6] L. Daniels, N. Belay, B.S. Rajagopal, P.J. Weimer, Bacterial methanogenesis and growth from CO2with elemental iron as the sole source of electrons, Science 237 (1987) 509-511.10.1126/science.237.4814.509

[7] J. Mand, H.S. Park, T.R. Jack, G. Voordouw, The role of acetogens in microbially influenced corrosion of steel, Frontiers in Microbiology 5 (2014) 1-1.10.3389/fmicb.2014.00268

[8] Y. Kryachko, S.M. Hemmingsen, The Role of Localized Acidity Generation in Microbially Influenced Corrosion, Current Microbiology 74 (2017) 870-876.10.1007/s00284-017-1254-6

[9] Y. Li, D. Xu, C. Chen, X. Li, R. Jia, D. Zhang, W. Sand, F. Wang, T. Gu, Anaerobic microbiologically influenced corrosion mechanisms interpreted using bioenergetics and bioelectrochemistry: A review, Journal of Materials Science and Technology 34 (2018) 1713-1718.10.1016/j.jmst.2018.02.023

[10] P.F. Beese-Vasbender, S. Nayak, A. Erbe, M. Stratmann, K.J.J. Mayrhofer, Electrochemical characterization of direct electron uptake in electrical microbially influenced corrosion of iron by the lithoautotrophic SRB Desulfopila corrodens strain IS4, Electrochimica Acta 167 (2015) 321-329.10.1016/j.electacta.2015.03.184

[11] G. Voordouw, P. Menon, T. Pinnock, M. Sharma, Y. Shen, A. Venturelli, J. Voordouw, A. Sexton, Use of Homogeneously-Sized Carbon Steel Ball Bearings to Study Microbially-Influenced Corrosion in Oil Field Samples, Frontiers in Microbiology 7 (2016).10.3389/fmicb.2016.00351

[12] S. Kakooei, M. Che Ismail, B. Ariwahjoedi, B.S. Iskandar, Mechanisms of Microbiologically Influenced Corrosion : A Review, World Applied Sciences Journal 17 (2012) 524-531

[13] H.T. Dinh, J. Kuever, M. Mußmann, A.W. Hassel, M. Stratmann, F. Widdel, Iron corrosion by novel anaerobic microorganisms, Nature 427 (2004) 829-832.10.1038/nature02321

[14] S. Kato, Microbial extracellular electron transfer and its relevance to iron corrosion, Microbial Biotechnology 9 (2016) 141-148.10.1111/1751-7915.12340

[15] K. Mori, H. Tsurumaru, S. Harayama, Iron corrosion activity of anaerobic hydrogen-consuming microorganisms isolated from oil facilities, Journal of Bioscience and Bioengineering 110 (2010) 426-430.10.1016/j.jbiosc.2010.04.012

[16] H. Tsurumaru, N. Ito, K. Mori, S. Wakai, T. Uchiyama, T. Iino, A. Hosoyama, H. Ataku, K. Nishijima, M. Mise, A. Shimizu, T. Harada, H. Horikawa, N. Ichikawa, T. Sekigawa, K. Jinno, S. Tanikawa, J. Yamazaki, K. Sasaki, S. Yamazaki, N. Fujita, S. Harayama, An extracellular [NiFe] hydrogenase mediating iron corrosion is encoded in a genetically unstable genomic island in Methanococcus maripaludis, Scientific Reports 8 (2018) 15149.10.1038/s41598-018-33541-5

[17] B.A. An, S. Kleinbub, O. Ozcan, A. Koerdt, Iron to Gas: Versatile Multiport Flow-Column Revealed Extremely High Corrosion Potential by Methanogen-Induced Microbiologically Influenced Corrosion (Mi-MIC), Front Microbiol 11 (2020) 527.10.3389/fmicb.2020.00527

[18] P.F. Beese-Vasbender, J.P. Grote, J. Garrelfs, M. Stratmann, K.J.J. Mayrhofer, Selective microbial electrosynthesis of methane by a pure culture of a marine lithoautotrophic archaeon, Bioelectrochemistry 102 (2015) 50-55.10.1016/j.bioelechem.2014.11.004

[19] P.A. Palacios, O. Snoeyenbos-West, C.R. Loscher, B. Thamdrup, A.E. Rotaru, Baltic Sea methanogens compete with acetogens for electrons from metallic iron, ISME J 13(12) (2019) 3011-3023.10.1038/s41396-019-0490-0

[20] P.A.P. Jaramillo, O. Snoeyenbos-West, C.R. Löscher, B. Thamdrup, A.-E. Rotaru, Baltic Methanosarcina and Clostridium compete for electrons from metallic iron, Biorxiv (2019) 1-26.10.1101/530386

[21] T. Uchiyama, K. Ito, K. Mori, H. Tsurumaru, S. Harayama, Iron-corroding methanogen isolated from a crude-oil storage tank, Appl Environ Microbiol 76(6) (2010) 1783-8.10.1128/AEM.00668-09

[22] N. Kip, S. Jansen, M.F.A. Leite, M. de Hollander, M. Afanasyev, E.E. Kuramae, J.A.V. Veen, Methanogens predominate in natural corrosion protective layers on metal sheet piles, Scientific Reports 7 (2017) 11899.10.1038/s41598-017-11244-7

[23] M.H. in 't Zandt, N. Kip, J. Frank, S. Jansen, J.A. van Veen, M.S.M. Jetten, C.U. Welte, High-Level Abundances of *Methanobacteriales* and *Syntrophobacterales* May Help To Prevent Corrosion of Metal Sheet Piles, Applied and Environmental Microbiology 85(20) (2019) e01369-19.10.1128/aem.01369-19

[24] R. Liang, R.S. Grizzle, K.E. Duncan, M.J. McInerney, J.M. Suflita, Roles of thermophilic thiosulfate-reducing bacteria and methanogenic archaea in the biocorrosion of oil pipelines, Frontiers in Microbiology 5 (2014) 1-12.10.3389/fmicb.2014.00089

[25] G. Joshi, Elucidating sweet corrosion scale, PhD thesis, The Univeristy of Manchester (2015)

[26] R. Barker, D. Burkle, T. Charpentier, H. Thompson, A. Neville, A review of iron carbonate (FeCO3) formation in the oil and gas industry, Corrosion Science 142 (2018) 312-341.10.1016/j.corsci.2018.07.021

[27] P. Refait, J.A. Bourdoiseau, M. Jeannin, D.D. Nguyen, A. Romaine, R. Sabot, Electrochemical formation of carbonated corrosion products on carbon steel in deaerated solutions, Electrochimica Acta 79 (2012) 210-217.https://doi.org/10.1016/j.electacta.2012.06.108

[28] B. Rasmussen, J.R. Muhling, Making magnetite late again: Evidence for widespread magnetite growth by thermal decomposition of siderite in Hamersley banded iron formations, Precambrian Research 306 (2018) 64-93.10.1016/j.precamres.2017.12.017

[29] A. Balows, The Prokaryotes : a handbook on the biology of bacteria : ecophysiology, isolation, identification, applications, Springer-Verlag, New York, 1992

[30] NACE, Standard Practice: Preparation, installation, analysis, and interpretation of corrosion coupons in oilfield operations. SP0775-2013, Item no. 21017, SP0775-201 (2013)

[31] N. International, Recommended Practice Preparation , Installation , Analysis , and Interpretation of Corrosion Coupons in Oilfield Operations, NACE Standard Recommended Practice (2005)

[32] M. Kubicek, G. Holzlechner, A.K. Opitz, S. Larisegger, H. Hutter, J. Fleig, A novel ToF-SIMS operation mode for sub 100nm lateral resolution: Application and performance, Applied Surface Science 289 (2014) 407-416.10.1016/j.apsusc.2013.10.177

[33] J.S. Deutzmann, M. Sahin, A.M. Spormann, Extracellular enzymes facilitate electron uptake in biocorrosion and bioelectrosynthesis, mBio 6(2) (2015).10.1128/mBio.00496-15

[34] S. Lahme, J. Mand, J. Longwell, R. Smith, D. Enning, Severe corrosion of carbon steel in oil field produced water can be linked to methanogenic archaea containing a special type of [NiFe] hydrogenase, bioRxiv (2020) 2020.07.23.219014.10.1101/2020.07.23.219014

[35] M. Mehanna, I. Rouvre, M.L. Delia, D. Feron, A. Bergel, R. Basseguy, Discerning different and opposite effects of hydrogenase on the corrosion of mild steel in the presence of phosphate species, Bioelectrochemistry 111 (2016) 31-40.10.1016/j.bioelechem.2016.04.005

[36] M.A. Pasek, J.M. Sampson, Z. Atlas, Redox chemistry in the phosphorus biogeochemical cycle, Proc Natl Acad Sci U S A 111(43) (2014) 15468-73.10.1073/pnas.1408134111

[37] Y. Tapia-Torres, G. Olmedo-Alvarez, Life on Phosphite: A Metagenomics Tale, Trends Microbiol 26(3) (2018) 170-172.10.1016/j.tim.2018.01.002

[38] G.E. Wood, A.K. Haydock, A. John, J.A. Leigh, Function and regulation of the formate dehydrogenase genes of the methanogenic archaeon Methanococcus maripaludis, Journal of Bacteriology 185 (2003) 2548-2554.10.1128/JB.185.8.2548

[39] M. Lienemann, J.S. Deutzmann, R.D. Milton, M. Sahin, A.M. Spormann, Mediator-free enzymatic electrosynthesis of formate by the Methanococcus maripaludis heterodisulfide reductase supercomplex, Bioresource Technology 254 (2018) 278-283.10.1016/j.biortech.2018.01.036

[40] D. Enning, H. Venzlaff, J. Garrelfs, H.T. Dinh, V. Meyer, K. Mayrhofer, A.W. Hassel, M. Stratmann, F. Widdel, Marine sulfate-reducing bacteria cause serious corrosion of iron under electroconductive biogenic mineral crust, Environmental Microbiology 14 (2012) 1772-1787.10.1111/j.1462-2920.2012.02778.x

[41] T. Borch, Y. Masue, R.K. Kukkadapu, S. Fendorf, Phosphate Imposed Limitations on Biological Reduction and Alteration of Ferrihydrite, Environmental Science and Technology 41(1) (2007) 166-172.DOI: 10.1021/es060695p

[42] V. Eroini, M.C. Oehler, B.K. Graver, A. Mitchell, K. L⊘nvik, T.L. Skovhus, Investigation of Amorphous Deposits and Potential Corrosion Mechanisms in Offshore Water Injection Systems, NACE International (2017) NACE-2017-9433

[43] S. Zheng, B. Wang, F. Liu, O. Wang, Magnetite production and transformation in the methanogenic consortia from coastal riverine sediments, J Microbiol 55(11) (2017) 862-870.10.1007/s12275-017-7104-1

[44] S. Kato, K. Hashimoto, K. Watanabe, Methanogenesis facilitated by electric syntrophy via (semi)conductive iron-oxide minerals, Environmental Microbiology 14 (2012) 1646-1654.10.1111/j.1462-2920.2011.02611.x

[45] O. Wang, S. Zheng, B. Wang, W. Wang, F. Liu, Necessity of electrically conductive pili for methanogenesis with magnetite stimulation, PeerJ 6 (2018) e4541.10.7717/peerj.4541

[46] Y. Yang, Removal Mechanisms of Protective Iron Carbonate Layer in Flowing Solutions, Chemical Engineering (Engineering and Technology), Ohio University, 2012, p. 188

[47] B. Ingham, M. Ko, N. Laycock, N.M. Kirby, D.E. Williams, First stages of siderite crystallisation during CO2 corrosion of steel evaluated using in situ synchrotron small- and wide-angle X-ray scattering, Faraday Discuss 180 (2015) 171-90.10.1039/c4fd00218k

Figure captions

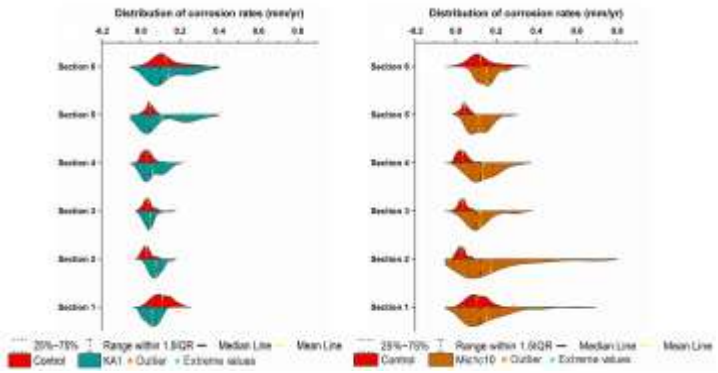

Figure 1: Corrosion rates distribution (mm/yr) of *M. maripaludis* KA1 (A; green area) and *M. maripaludis* Mic1c10 (B; orange area) along the different sections (1-6) compared with abiotic control (red areas). Each column was separated using glass beads. The multiport-flow columns (MFC) were incubated with *M. maripaludis* KA1 or *M. maripaludis* Mic1c10 without flow (3.5 days). Post incubation, fresh artificial seawater was continuously injected into MFCs for 14 days. Individual bead corrosion rates for biological replicates (N=3) were compared against abiotic control in the forms of corrosion rate distribution, mean, median and outliers.

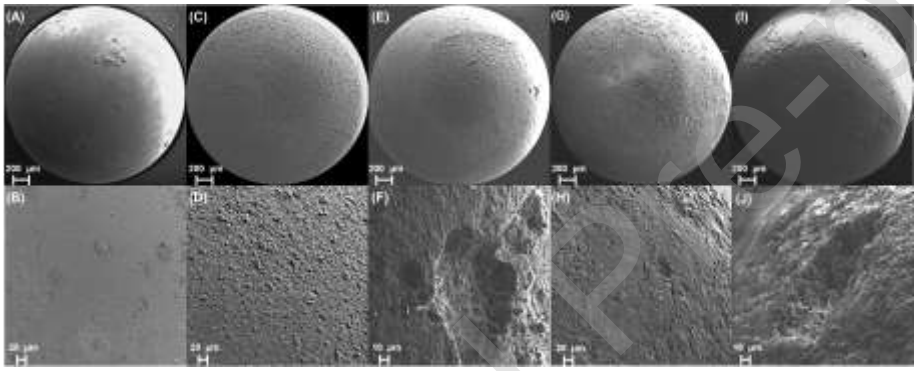

Figure 2 SEM micrographs of the most-corroded carbon steel beads from *M. maripaludis* KA1 (C-F) and *M. maripaludis* Mic1c10 (G-J), in comparison to non-corroded beads (A and B). Carbon steel beads with corrosion rates 0.36 mm/yr (C and D) and 0.38 mm/yr (E and F) of *M. maripaludis* KA1 and beads with corrosion rates 0.60 mm/yr (G and H) and 0.72 mm/yr (I and J) are shown.

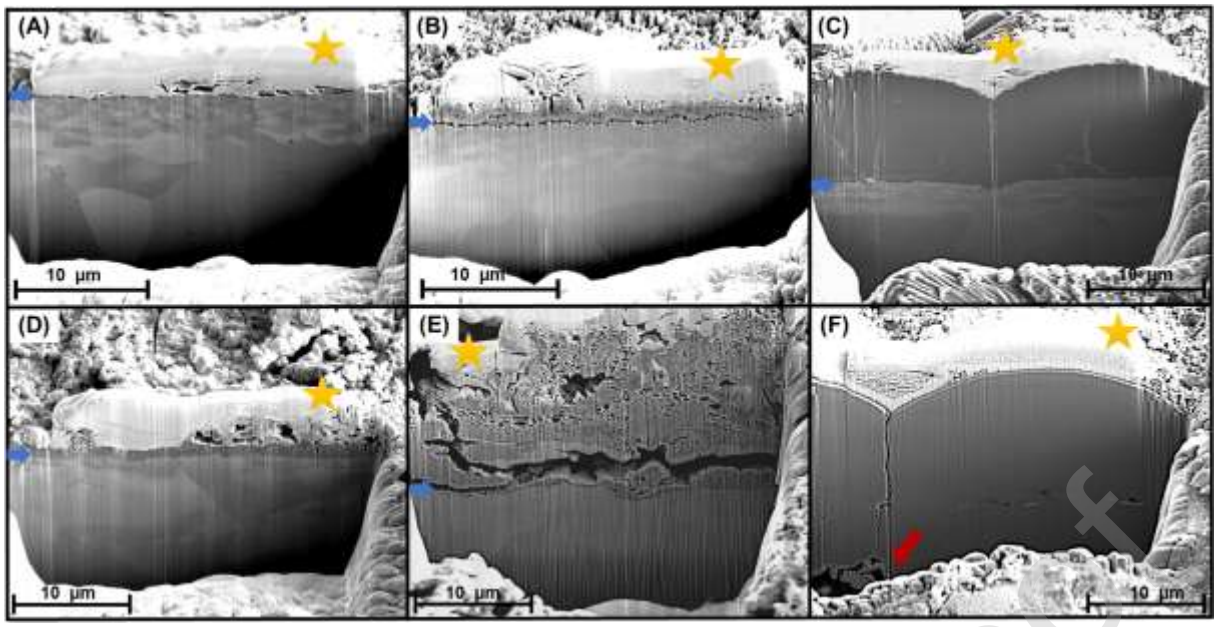

Figure 3: Images taken by Focused-ion beam scanning electron microscope (FIB-SEM) of control (A and D), *M. maripaludis* KA1 (B and E) and *M. maripaludis* Mic1c10 (C and F). Coupons from static incubations (top row) and flow column (bottom row) are shown. Yellow stars indicate platinum deposits. Blue arrows indicate the line separating the corrosion product and the iron surface. Red arrow indicates a porous layer between the carbon steel coupon and the compact corrosion layer.

Figure 4: Images of the coupon incubated for 14 days with *M. maripaludis* KA1 in the column system by secondary electron micrograph and SEM-EDS. (A) Secondary electron micrograph of the coupon cross-section. The solid, light grey structure on the bottom is the metal substrate, the light grey structure above is the corrosion layer embedded in the epoxy resin (dark grey). (B-H) SEM-EDS images for the relevant elements.

Figure 5: Images of the coupon incubated for 14 days with *M. maripaludis* KA1 in the static culture by secondary electron micrograph and SEM-EDS. (A) Secondary electron micrograph image of the coupon cross-section. The solid, light grey structure on the bottom is the metal substrate, the grey structure above is the corrosion layer embedded in the epoxy resin (dark grey). (B-H) SEM-EDS images for the relevant elements.

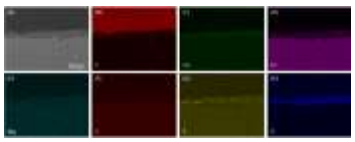

Figure 6: Images of the coupon for 14 days with *M. maripaludis* Mic1c10 in the column system by secondary electron micrograph and SEM-EDS. (A) Secondary electron micrograph image of the coupon cross-section. The solid, light grey structure on the bottom is the metal substrate, the grey structure above is the corrosion layer embedded in the epoxy resin (dark grey). (B-H) SEM-EDS images for the relevant elements.

Figure 7: Images of the coupon incubated for 14 days with *M. maripaludis* Mic1c10 in the static culture by secondary electron micrograph and SEM-EDS. (A) Secondary electron micrograph image of the coupon cross-section. The solid, light grey structure on the bottom is the metal substrate, the grey structure above is the corrosion layer embedded in the epoxy resin (dark grey). (B-H) SEM-EDS images for the relevant elements.

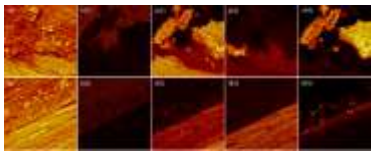

Figure 8 ToF-SIMS images acquired in the negative mode of carbon steel coupon cross-sections incubated with *M. maripaludis* KA1 (A-B). All images have a 100x100 µm² FoV and are normalized to the total ion intensity. (A) Total ion image of the cross-section KA1 coupon from the column system, (A1) m/z = 12, $C^{-,}$ (A2) m/z = 16, O^-, (A3) m/z = 32, O^{2-} or S^- and (A4) m/z = 63, PO^{2-}. (B) Total ion image of the cross-section KA1 coupon from the static culture, (B1) m/z = 12, C^-, (B2) m/z = 16, O^-, (B3) m/z = 32, O^{2-} or S^-, and (B4) m/z = 63, PO^{2-}.

Figure 9 ToF-SIMS images acquired in the negative mode of carbon steel coupon cross-sections incubated with *M. maripaludis* Mic1c10 (A-B). All images have a 100x100 µm² FoV and normalized to the total ion intensity. (A) Total ion image of the cross-section Mic1c10 coupon from the column system, (A1) m/z = 12, C^-, (A2) m/z = 16, O^-, (A3) m/z = 32, O^{2-} or S^- and (A4) m/z = 63, PO^{2-}. (B) Total ion image of the cross-section Mic1c10 coupon from the static culture, (B1) m/z = 12, C^-, (B1) m/z = 16, O^-, (B3) m/z = 32, O^{2-} or S^- and (B4) m/z = 63, PO^{2-}.

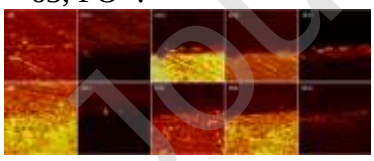

Figure 10 ToF-SIMS images acquired in the negative mode of carbon steel coupon cross-sections of abiotic control (A-B). All images have a 100x100 µm² FoV and normalized to the total ion intensity. (A) Total ion image of the cross-section abiotic control coupon from the column system, (A1) m/z = 12, C^-, (A2) m/z = 16, O^-, (A3) m/z = 32, O^{2-} or S^- and (A4) m/z = 63, PO^{2-}. (B) Total ion image of the cross-section Mic1c10 coupon from the static culture, (B1) m/z = 12, C^-, (B2) m/z = 16, O^-, (B3) m/z = 32, O^{2-} or S^- and (B4) m/z = 63, PO^{2-}.

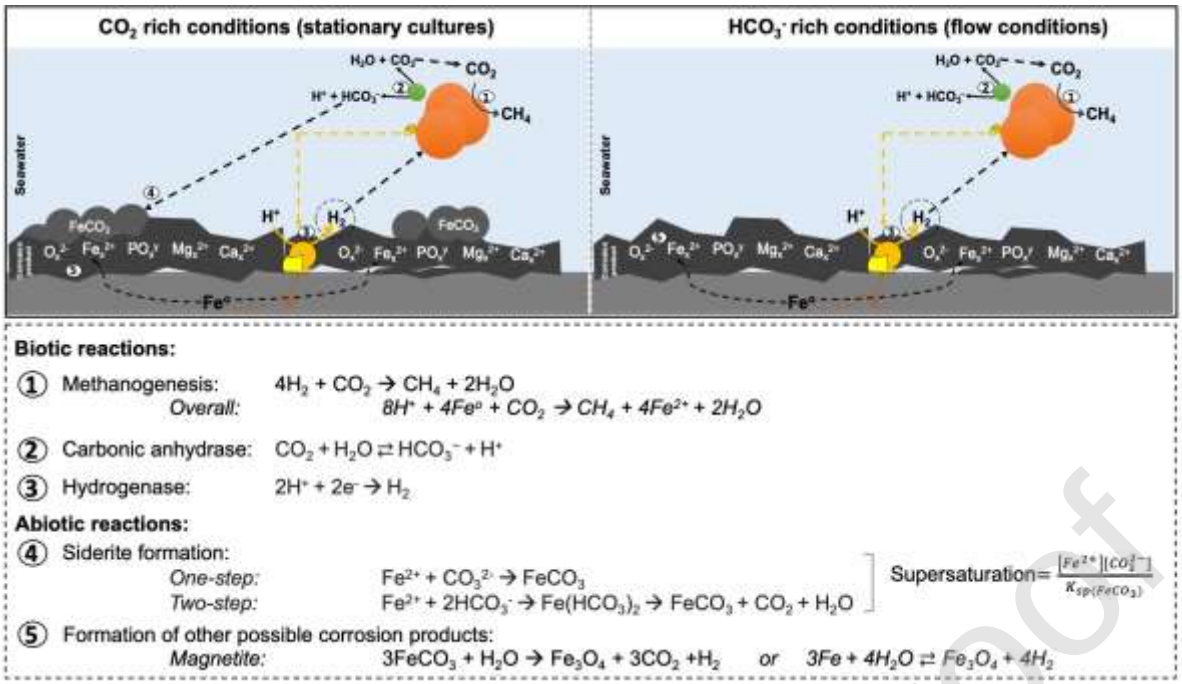

Figure 11 Schematic overview of microbiologically influenced corrosion by methanogens (Mi-MIC) in neutral seawater conditions. Possible biotic and abiotic reactions involved are also shown. Please note, the reactions illustrated may occur simultaneously and only the reactions of Mi-MIC are shown. Specialized adaptations of corrosive *Methanococcus maripaludis* strains are shown in reactions 1 to 3, secretion of redox enzymes, such as hydrogenases (3), produce the hydrogen needed for methanogenesis (1). Carbonic anhydrase will then convert between bicarbonate and carbon dioxide when needed for methanogenesis (2). Previously proposed corrosion product of Mi-MIC is siderite ($FeCO_3$) is formed through two different pathways (4), and strictly dependent on the supersaturation of crystal nucleation. Presence of siderite was not detected in low CO_2 or rich HCO_3^- conditions, i.e. flow conditions, due to the conversion of HCO_3^- into CO_2 for methanogenesis. Other corrosion products of Mi-MIC may form (5), though the specific orientation and crystallized forms are unknown.